# Odd dynamics of living chiral crystals

https://doi.org/10.1038/s41586-022-04889-6

Received: 16 May 2021

Accepted: 20 May 2022

Published online: 13 July 2022

Check for updates

Tzer Han Tan<sup>1,2,3,5</sup>, Alexander Mietke<sup>4,5</sup>, Junang Li<sup>1</sup>, Yuchao Chen<sup>1</sup>, Hugh Higinbotham<sup>1</sup>, Peter J. Foster¹, Shrevas Gokhale¹, Jörn Dunkel⁴ & Nikta Fakhri¹⊠

Active crystals are highly ordered structures that emerge from the self-organization of motile objects, and have been widely studied in synthetic<sup>1,2</sup> and bacterial<sup>3,4</sup> active matter. Whether persistent crystalline order can emerge in groups of autonomously developing multicellular organisms is currently unknown. Here we show that swimming starfish embryos spontaneously assemble into chiral crystals that span thousands of spinning organisms and persist for tens of hours. Combining experiments, theory and simulations, we demonstrate that the formation, dynamics and dissolution of these living crystals are controlled by the hydrodynamic properties and the natural development of embryos. Remarkably, living chiral crystals exhibit self-sustained chiral oscillations as well as various unconventional deformation response behaviours recently predicted for odd elastic materials<sup>5,6</sup>. Our results provide direct experimental evidence for how non-reciprocal interactions between autonomous multicellular components may facilitate non-equilibrium phases of chiral active matter.

Symmetry breaking<sup>7,8</sup> is a hallmark of living<sup>9</sup> and synthetic<sup>1,10-12</sup> active matter. From the asymmetric growth of multicellular organisms 9,13,14 to the coherent motions of swimming cells<sup>15,16</sup> and self-propelled colloids<sup>1,10,17,18</sup>, active systems form self-organized structures<sup>19–21</sup> with unusual material properties<sup>22-24</sup> that can only emerge far from thermal equilibrium. Despite major experimental<sup>1,3,10,16,18,23</sup> and theoretical<sup>25-27</sup> progress over the past decade, we are only beginning to understand how complex collective behaviours of multicell  $\bar{u}lar^{28-\bar{3}1}$  and multiorganisms.  $mal^{32,33}$  systems arise from the broken symmetries and non-equilibrium dynamics of their individual constituents.

Aparticularly interesting class of non-equilibrium symmetry-breaking phenomena comprises the active crystallization processes recently observed in colloidal<sup>1</sup> and bacterial<sup>3</sup> systems. Unlike conventional passive crystals, which form on lowering the temperature and often require attractive forces, active crystallization arises from the particles' self-propulsion and can occur even in purely repulsive dilute systems<sup>1</sup>. A long-standing, related, unanswered question is whether groups of multicellular organisms can self-organize into states of crystalline order and, if so, what emergent material properties they might exhibit.

Here we report the observation of spontaneous crystallization in large assemblies of developing starfish Patiria miniata embryos (Fig. 1a and Supplementary Video 1). Our experimental observations show how, over the course of their natural development, thousands of swimming embryos come together to form living chiral crystal (LCC) structures that persist for many hours (Supplementary Video 1). In contrast to externally actuated colloidal systems, the self-assembly, dynamics and dissolution of these LCCs are controlled entirely by the embryos' internal developmental programme (Fig. 1a,b). A quantitative theoretical analysis reveals that LCC formation arises from the complex hydrodynamic interactions 34,35 between the starfish embryos. Once formed, these LCCs exhibit striking collective dynamics, consistent with predictions from a recently proposed theory of odd elasticity<sup>5</sup>.

#### Self-assembly and dissolution of LCCs

During early development, starfish embryos exhibit substantial morphological changes. From the onset of gastrulation (Fig. 1b, 0h), embryos elongate along their anterior-posterior (AP) axis (0-44 h) while progressively developing folds that further break shape symmetry. In parallel, the self-generated fluid flow near the embryo's surface changes (Fig. 1b), reflecting spatial reconfigurations of cilia during growth<sup>36</sup> similar to other ciliated organisms<sup>37</sup>. Similarly to hydrodynamically bound 'dancing' Volvox algae 34, when starfish embryos come close to the fluid surface, they can attain a stable bound state in which their AP axes are oriented perpendicular to the fluid-air interface. Groups of surface-bound embryos can spontaneously self-organize into two-dimensional hexagonal clusters (Fig. 1a, 2-5 h, and Supplementary Video 1). Over time, these clusters grow into larger crystals, reaching sizes of hundreds to thousands of embryos (Fig. 1a, 26 h) and persisting for tens of hours. As embryos develop further (Fig. 1b, 38-44 h) crystals begin to disassemble (Fig. 1a, 35 h) and eventually dissolve completely (Fig. 1a, 38 h).

Viewed from above, both small and large crystals rotate clockwise (Fig. 1c and Supplementary Video 2), consistent with the chiral spinning motions of individual embryos about their AP axis (Fig. 2a). Large LCCs typically exhibit a high degree of hexagonal order, while also harbouring lattice defects (Fig. 1d). The assembly, rotational dynamics and dissolution of LCCs can be rationalized by a hydrodynamic analysis that accounts for the flow fields generated by individual embryos (Figs. 1e and 2a-c).

### Hydrodynamic theory of LCCs

To understand the hydrodynamic interactions underlying the cluster dynamics, we first analysed the fluid flow around individual embryos bound below the air-water interface (Fig. 2a,b). Observed along the

Department of Physics, Massachusetts Institute of Technology, Cambridge, MA, USA. <sup>2</sup>Quantitative Biology Initiative, Harvard University, Cambridge, MA, USA. <sup>3</sup>Center for Systems Biology Dresden, Dresden, Germany. <sup>4</sup>Department of Mathematics, Massachusetts Institute of Technology, Cambridge, MA, USA. <sup>5</sup>These authors contributed equally: Tzer Han Tan, Alexander Mietke. <sup>™</sup>e-mail: fakhri@mit.edu

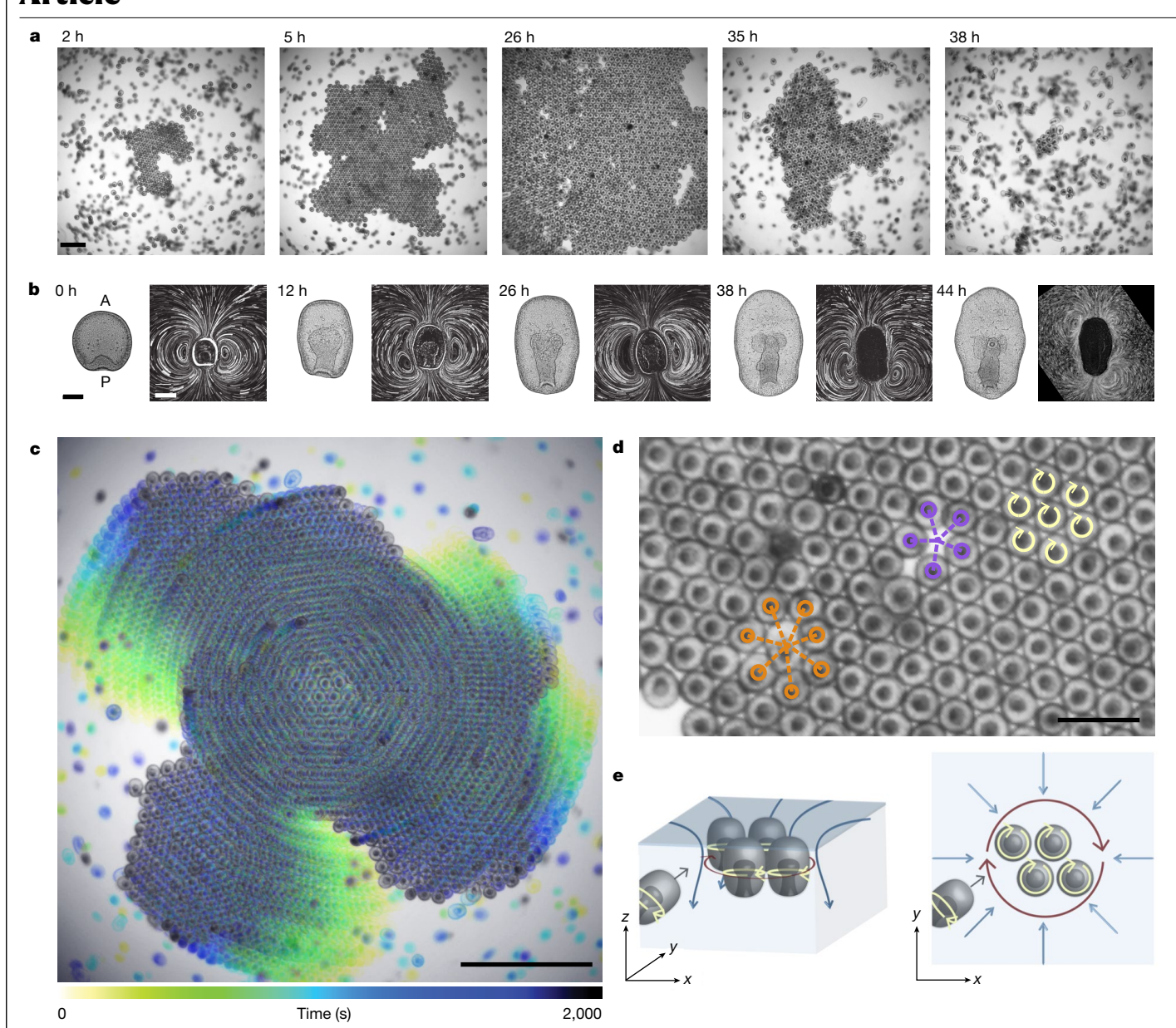


**Fig. 1**| **Developing starfish embryos self-organize into living chiral crystals. a**, Time sequence of still images showing crystal assembly and dissolution (Supplementary Video 1). t = 0 h corresponds to the onset of clustering. Scale bar, 1 mm. **b**, Embryo morphology (left) and flow fields (right) change with developmental time. Shape scale bar, 100  $\mu$ m. Flow-field scale bar, 200  $\mu$ m. See Supplementary Information for uncropped morphology images. **c**, Embryos assembled in a crystal perform a global collective rotation (Supplementary

 $Video\ 2). Scale\ bar,\ 2\ mm.\ \textbf{d},\ Spinning\ embryos\ (yellow\ arrows)\ in the\ crystal\ form\ a\ hexagonal\ lattice,\ containing\ fivefold\ (purple)\ and\ sevenfold\ (orange)\ defects.\ Scale\ bar,\ 0.5\ mm.\ \textbf{e},\ Schematic\ of\ embryo\ dynamics\ and\ fluid\ flows\ from\ side\ view\ (left)\ and\ top\ view\ (right).\ Crystals\ of\ spinning\ embryos\ form\ near\ the\ air-water\ interface.\ Self-generated\ hydrodynamic\ flows\ lead\ to\ an\ effective\ attraction\ between\ surface-bound\ embryos\ .\ Blue\ arrows\ depict\ fluid\ flows,\ dark\ red\ arrows\ indicate\ rotations\ of\ groups\ of\ embryos\ .$ 

AP axis, fluid moves radially inwards towards the embryo, reaches a maximum speed of 0.1–0.2 mm s $^{-1}$  lateral to the embryo surface (Fig. 2b), and eventually moves towards the bottom of the well (Fig. 1e). The radial in-flow generated by isolated embryos can be described as a Stokeslet flow  $^{34}$  (Fig. 2b, blue curve), a solution of the Stokes equation that describes the generic fluid flow around an external force (Supplementary Section 3.2.2). This force is related to the negative buoyancy of embryos. Indeed, the buoyant weight force  $F_{\rm g}$  = 1.7  $\pm$  0.4 nN estimated from sedimentation speeds of immobilized embryos  $^{34}$  (Supplementary Section 1.4) is close to the Stokeslet strength  $F_{\rm st}$  = 2.6  $\pm$  0.3 nN obtained from fitting radial in-plane flow fields (Fig. 1b and Supplementary Section 2.1.6).

Theself-generated Stokeslet flow stabilizes the upright AP-axis orientation of embryos below the fluid surface (Supplementary Section 2.1.6). In addition, it induces an effective long-ranged hydrodynamic

attraction between embryos, facilitating the assembly of clusters. Similar effects have been observed previously for bacterial and algal microswimmers near rigid surfaces<sup>3,34</sup>. Once two embryos are close together, their intrinsic spinning motions lead to an additional exchange of hydrodynamic forces and torques (Fig. 2d). Similar to pairs of *Volvox* colonies near a rigid surface<sup>34,38</sup>, nearby starfish embryos orbit each other, and their spinning frequency decreases compared with that of a freely spinning embryo. The excess cilia-generated torque from slower-rotating embryos<sup>34</sup> manifests itself in systematic azimuthal flow contributions (Fig. 2c). To confirm our understanding of these hydrodynamic interactions, we complemented the Stokeslet flow of each embryo with additional contributions that reflect the effects of hydrodynamic interactions (Supplementary Section 3.2.2 and Supplementary Fig. 5). Flow fields

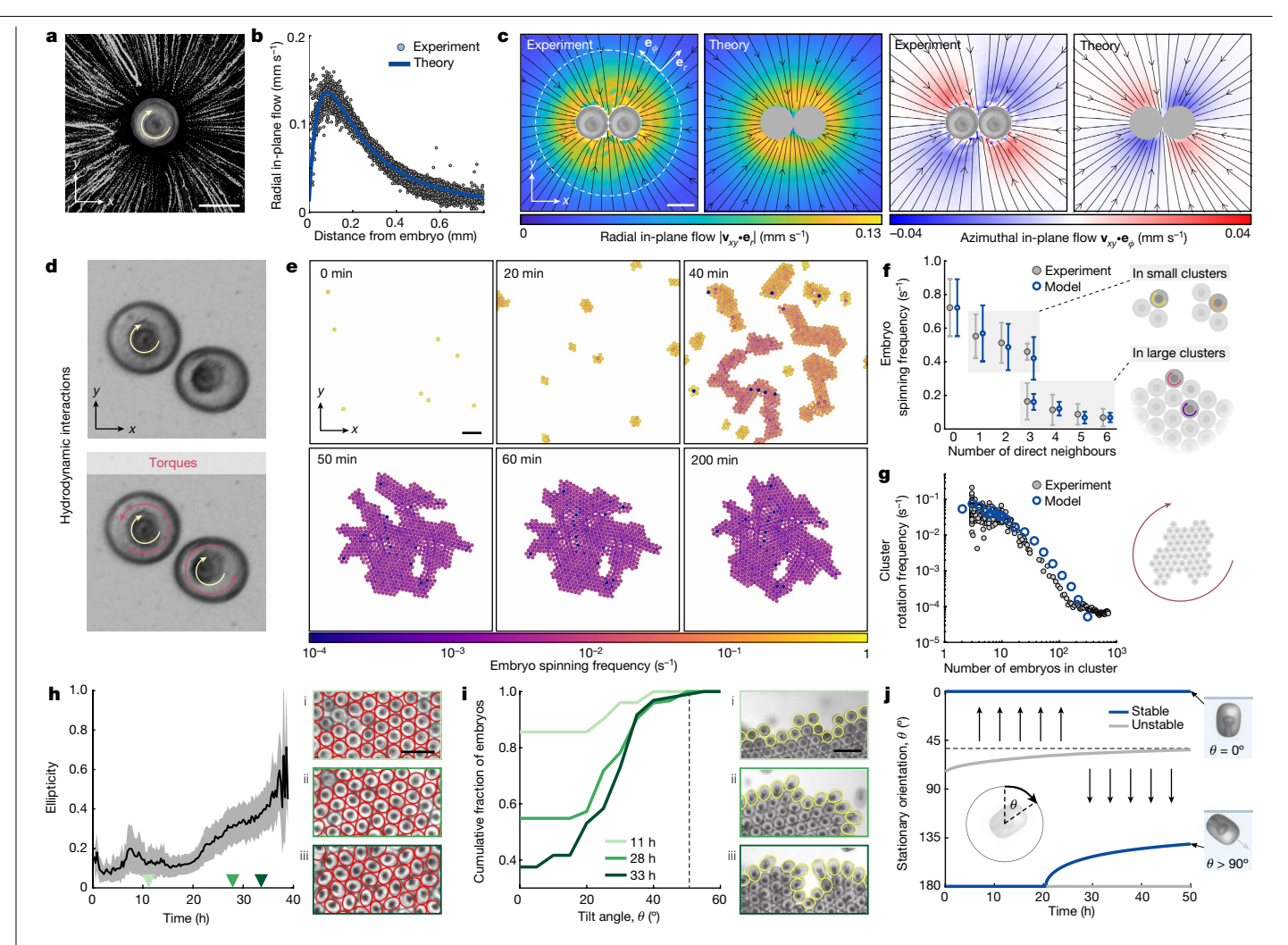


Fig. 2 | Single-embryo properties facilitate formation, rotations and dissolution of clusters. a, Top view of a single embryo. The arrows indicate the spinning direction and the dotted lines visualize the streamlines  $(Supplementary Section 1.2). \, \boldsymbol{b}, Measured \, radial \, in-flow \, velocities \, (grey \, dots)$ are well described by Stokeslet flow below a free surface (blue line) (Supplementary Section 2.1.6). c, In-plane flows  $\mathbf{v}_{xy}$  surrounding bound pairs (experiment; Supplementary Video 3 and Supplementary Section 3.2.1) fitted by a solution of the Stokes equation (theory; Supplementary Section 3.2.2) taking into account hydrodynamic interactions (d).  $\mathbf{e}_r$  and  $\mathbf{e}_{\phi}$  denote radial and azimuthal basis vectors, respectively.  $\mathbf{d}$ , Hydrodynamic interactions cause nearby embryos to orbit each other and reduce individual spinning frequencies. Yellow arrows indicate embryo rotations. Brown and red arrows depict effective forces and torques due to hydrodynamic interactions. e. Stokeslet-mediated attraction (a.b) and hydrodynamic near-field interactions of spinning particles (d) in an experimentally constrained minimal model (Supplementary Section 2.2) reproduce crystal formation as seen in

small (≤4 embryos) and large (about 100 embryos) clusters. The error bars denote standard deviations of measurements (experiment) and simulations (model) (Supplementary Section 2.2.3). g, Cluster-size dependent reduction of  $individual\,embryo's\,spinning\,activity\,(Supplementary\,Section\,2.2.2)\,leads\,to$ good agreement with measured whole-cluster rotation frequencies. **h**, Ellipticity of embryo shapes (right: top-view outlines in red; Supplementary Section 3.5) increases during development, leading to increasingly noisy steric interactions among spinning embryos in clusters. The grey band depicts standard deviation. i, Embryos at cluster boundaries exhibit progressively increasing AP-axis tilt angles (right: projection outlines in yellow; Supplementary Section 3.5). The dashed line indicates the critical angle at which bound states of late embryos become unstable. j, Stationary orientations and stability of microswimmers with hydrodynamic properties akin to developing embryos (Supplementary Sections 2.1.1-2.1.5). A decreasing critical angle (grey line) and the increase in effective noise (h,i) increase the rate of embryos leaving cluster boundary and fluid surface, ultimately driving clusters dissolution. Scale bars, 200  $\mu$ m (**a**,**c**), 100  $\mu$ m (**d**), 1 mm (**e**) and 500  $\mu$ m (**h**,**i**).

fitted via this approach show good quantitative agreement with experimental measurements (Fig. 2c and Supplementary Fig. 6).

experiments (Supplementary Video 4). f, Single-embryo spinning frequencies in

On the basis of these insights, we experimentally constrained a minimal model in which upright spinning embryos are represented by rigid disks interacting through hydrodynamic Stokeslet-mediated pairwise attraction, and through pairwise transverse force and torque exchanges (Supplementary Section 2.2). Using the Stokeslet strength determined from fits as in Fig. 2b, and a parameterization of transverse interactions based on rotation frequency measurements of bound pairs and triplets (Supplementary Section 2.2.2), this minimal model predicts the self-organized formation of rotating clusters similar to those seen in the experiments (Fig. 2e and

Supplementary Video 4). Assuming a cluster-size dependent reduction of the individual embryo's spinning activity to match whole-cluster rotation rates (Supplementary Section 2.2.2), the model quantitatively captures the experimentally observed reduction of individual embryo rotation frequencies in both small and large clusters (Fig. 2f), as well as their collective translation into global cluster rotation rates (Fig. 2g).

To investigate how developmental changes of embryos contribute to the dissolution of a cluster, we followed the time-dependent morphology and hydrodynamics of embryos. Body-shape anisotropies perpendicular to the AP axis increase almost fivefold over the course of experiments (Fig. 2h). Such anisotropies cause neighbouring embryos

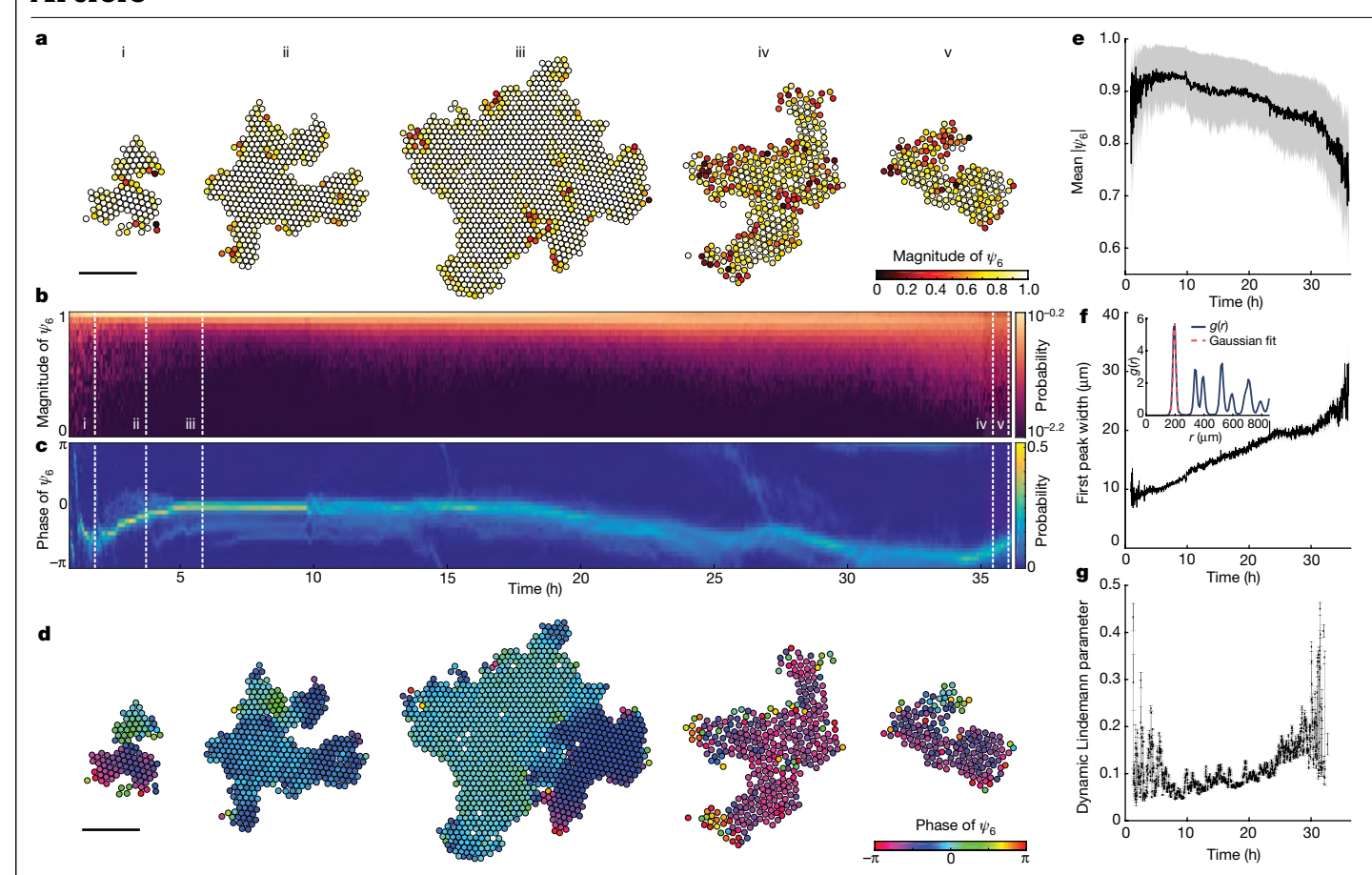


**Fig. 3** | **Crystalline order first increases and then decreases as embryos develop. a**, Embryo centroids at different time points colour-coded by the magnitude of the orientational order parameter  $|\psi_6|$  (Supplementary Section 3.6 and Supplementary Video 5). Scale bar, 2 mm. **b.c.** The measured probability distribution of  $|\psi_6|$  spreads to smaller values after about 20 h, indicating a loss of bond-orientational order (b). The ensuing drift of the mean phase angle (c) signals dynamical restructuring of the crystal. **d**, Embryo centroids at different times colour-coded by the phase of  $\psi_6$ . Scale bar, 2 mm. Time slices corresponding to snapshots (i)–(v) in **a** and **d** are indicated by white dotted lines. **e**, Average magnitude of  $\psi_6$  decays after about 10 h, confirming a

decrease in orientational order. The error bars indicate the standard deviation.  $\mathbf{f}$ , The widening of the first peak of the radial pair distribution function  $\mathbf{g}(r)$  indicates increased variation in the distance between nearest neighbours. The error bars indicate the 95% confidence interval from a Gaussian fit. Inset: example pair distribution function,  $\mathbf{g}(r)$ , and Gaussian fit to the first peak (Supplementary Section 3.7).  $\mathbf{g}$ , The increase of the dynamic Lindemann parameter with developmental time signals a progressive destabilization of the crystal lattice. The error bars indicate the standard deviation of 20 consecutive time points (Supplementary Section 3.8).

to 'bump' into each other when closely packed and spinning within a cluster, introducing an effective source of noise in the LCC lattice. The increased interaction noise is particularly visible at cluster boundaries, where embryos become increasingly tilted as their morphological development progresses (Fig. 2i), increasing their tendency to leave or to be scattered off a cluster. Using additional flow-field measurements of single embryos at different time points (Supplementary Section 3.3), we parameterized an orientational stability diagram that reveals a bistable nature of bound-state orientations (Fig. 2j and Supplementary Section 2.1). In addition to a stable upright orientation ( $\theta = 0^{\circ}$ , where  $\theta$  is defined in the Fig. 2j inset), downwards-oriented stable orientations ( $\theta > 90^{\circ}$ ) exist for which embryos are expected to swim away from the surface. These two orientations are separated by an unstable critical angle (Fig. 2j, grey). The increase of effective noise as characterized in Fig. 2j,h contributes to an increased rate at which embryos tilt beyond this critical angle and therefore represents a key factor in the eventual dissolution of clusters.

#### Temporal evolution of crystalline order

A striking feature of the LCCs is that they nucleate, grow and dissolve naturally as embryos progressively develop (Fig. 1a and Supplementary

Video 1). To quantify the evolution of crystalline order, we calculated the local order parameter  $\psi_6(\mathbf{r}_i) = |\psi_6|_e^{i\phi_i}$  where i is the imaginary number and  $\mathbf{r}_i$  denotes embryo positions in the co-rotating frame of the cluster (Supplementary Sections 3.1 and 3.6). Measurements of  $\psi_6(\mathbf{r}_i)$  determine the local phase  $\phi_i$  representing the crystal orientation, as well as the magnitude of hexagonal order  $|\psi_6|_i$  (ref.  $^{39}$ ). Initially, small clusters merge together along different crystal axes, resulting in grain boundaries and broad distributions of  $|\psi_6|_i$  and  $\phi_i$  (Fig. 3a–d(i) and Supplementary Video 5). Within 5 h of crystal formation, LCCs undergo rapid internal restructuring, during which subdomains align. This results in large, nearly defect-free crystals with a high degree of hexagonal order ( $\langle |\psi_6|_i \rangle \approx 0.9$ ) and a narrow distribution of local bond orientation (Fig. 3a–d(ii),(iii)). This highly ordered state persists for several hours.

As development progresses, changes in morphology and surrounding flow fields (Figs. 1b and 2h) lead to a decreased crystalline order. Specifically, the probability density of  $|\psi_6|_i$  spreads to smaller values (Fig. 3b,e, t > 20 h), quantitatively indicating a loss of orientational order. A similar spread is observed in the average phase angle  $\phi_i$ , indicating the loss of a well defined, global crystal orientation (Fig. 3c, t > 20 h). After about 30 h, disorder dominates and the crystal dissolves over a period of 10 h (Fig. 3a–d(iv),(v)).

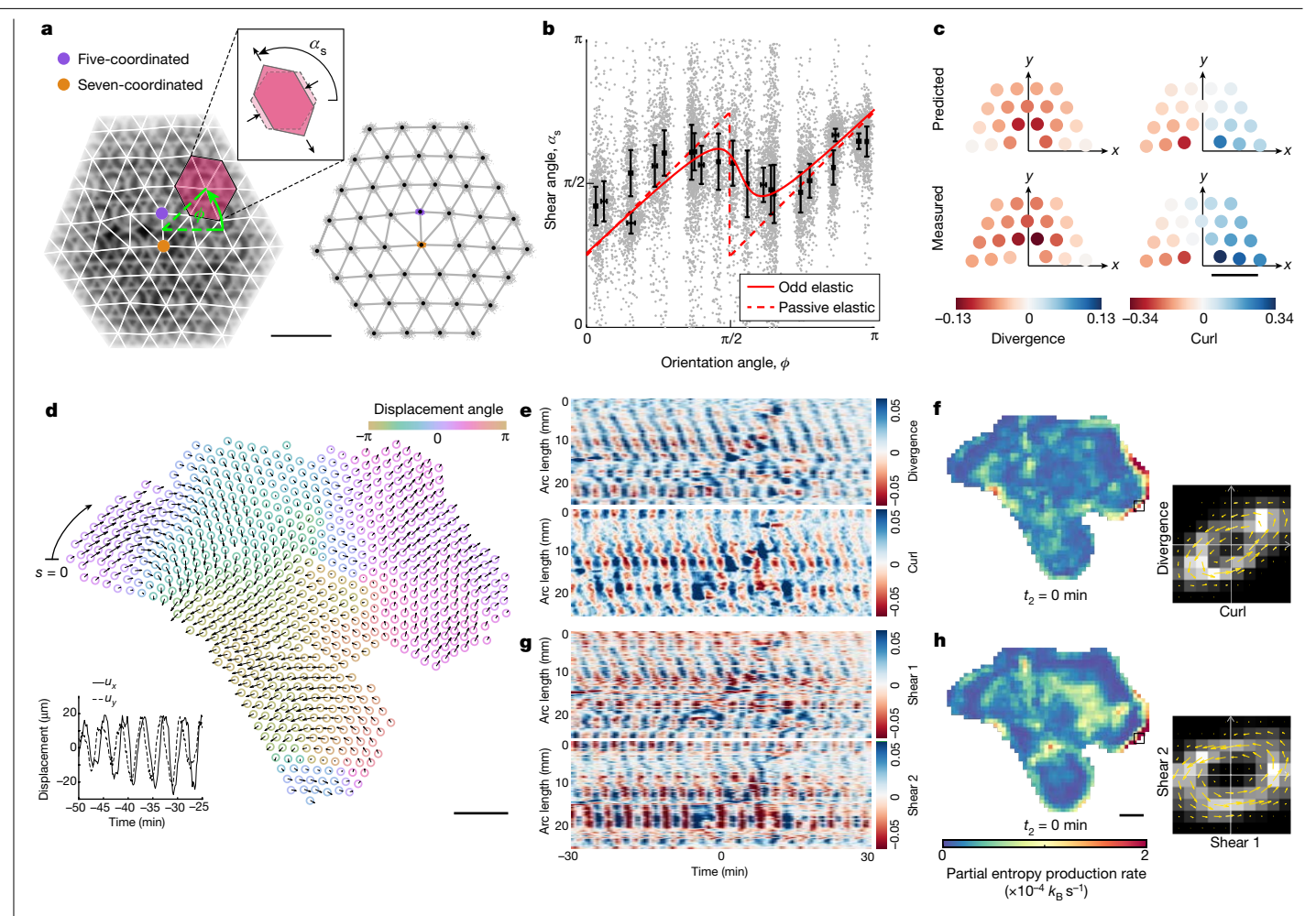


Fig. 4 | Defect strains and displacement waves exhibit signatures of odd **elasticity. a**, Shear-strain angles  $\alpha_s$  near a defect—defined by a pair of embryos with five (purple) and seven (orange) neighbours-encode information about effective material properties. Left: Delaunay triangulation overlaid with a crystal. Right: embryo centroid positions (grey dots) collected over 80 min; the black dots depict average positions identified as lattice sites (Supplementary Section 3.11.1). Scale bar, 500  $\mu$ m. **b**, Measured shear angle  $\alpha_s$  seen along  $\phi$  for the data in a (grey dots) and averages at lattice sites (black symbols; the error bars depict standard deviation). Dashed line,  $\alpha_s(\phi)$  predicted for passive elastic solids (no fit parameter). Solid line, best fit including contributions from an isotropic odd elastic solid<sup>6</sup> (Supplementary Section 3.11.4). c, Odd elastic moduli obtained from fits of spatial shear-strain profiles predict measured divergence and curl strain components with good quantitative agreement (Supplementary Section 3.11.5). Scale bar, 500 μm. **d**, Snapshot of embryo

displacements during cluster oscillations (Supplementary Section 3.9). Inset: x- and y-displacement components of a representative embryo indicate robust oscillations with a frequency of about 0.26 min<sup>-1</sup> (Supplementary Video 7). Scale bar, 1 mm. e, Space-time kymographs of the strain components divergence and curl along the boundary (Supplementary Section 3.9). Oscillations with similar amplitude are also present in the bulk (Supplementary Fig. 10). f, Spatial map of the partial entropy production rate computed in the strain component space of curl and divergence.  $k_B$  denotes the Boltzmann constant. (Supplementary Section 3.12.1 and Supplementary Video 10). Scale bar, 1 mm. Inset: probability density current in the curl-divergence strain component space computed at the location of the black box shows a representative anticlockwise strain cycle (Supplementary Section 3.12.2). g,h, An analogous analysis in the shear-strain component space yields similar results to e and f, respectively.

Furthermore, we identified a progressive loss of translational order before dissolution as quantified by the radial pair distribution function g(r) (inset in Fig. 3f and Supplementary Section 3.7). Specifically, the first peak width of g(r) – representing the variability of nearest-neighbour distances—was found to increase with development (Fig. 3f). Consequently, deviations from an ideal hexagonal lattice become more frequent and translational order is reduced as embryos develop.

To examine whether the evolution of orientational and translational order is also reflected in dynamic crystal properties, we determined the dynamic Lindemann parameter (Supplementary Section 3.8), which characterizes the strength of fluctuations in the crystal lattice<sup>40</sup>. In the crystalline phase (5–25 h), the dynamic Lindemann parameter increases with time (Fig. 3g) and indicates a progressive destabilization of the crystal lattice, consistent with the observed loss of orientational (Fig. 3e) and translational order (Fig. 3f), and with the increased

interaction noise due to changes in the embryo morphology (Fig. 2h,i). Large fluctuations of the dynamic Lindemann parameter at early and late times are due to the small crystal sizes and the highly dynamic nature of growing and dissolving clusters.

Taken together, the systematic decay of orientational, translational and dynamic order with developmental time shows how morphological changes at the single-embryo level (Figs. 1b and 2h) can autonomously drive LCCs through a dissolution transition reminiscent of solid-gas phase transitions.

#### Odd elasticity and emergent chiral waves

Starfish embryos are inherently chiral and spin about their AP axis in a left-handed manner (Figs. 1d and 2a). This chiral spinning motion leads to distance-dependent, transverse lubrication interactions between pairs of

embryos (Fig. 2d). A coarse-graining of our minimal model (Supplementary Section 2.3) suggests that these interactions could lead to effective material properties of LCCs that emulate an odd elastic material  $^{5.6}$ . Odd elasticity theory complements the conventional elastic response of passive isotropic solids to compression and shear—a bulk modulus B and a shear modulus  $\mu$ —by odd bulk and shear moduli A and  $K^{\circ}$ , respectively. Odd elasticity can emerge in active isotropic solids that are chiral A.

To identify signatures of odd elasticity in our experimental data, we use the fact that LCCs typically harbour lattice defects (Figs. 1d and 4a, and Supplementary Video 6). The defects locally deform LCCs, with the deformation field encoding information about the effective material properties. We quantify deformations in the frame co-rotating with the cluster by measuring the displacement  $\mathbf{u}(\mathbf{r}_i, t) = (u_x, u_y)^T$  of embryos at position **r**<sub>i</sub> and time *t* from a regular lattice (Supplementary Section 3.9). By computing the displacement gradient tensor  $u_{ij} = \partial_i u_i (i, j \in \{x, y\})$ (Supplementary Sections 3.9 and 3.11), relative deformations can be expressed in terms of four strain components<sup>5</sup>: divergence  $(u^0 = u_{xx} + u_{yy})$ , curl/rotations  $(u^1 = u_{yx} - u_{xy})$  and shear-strain components 'shear 1'  $(u^2 = u_{xx} - u_{yy})$  and 'shear 2'  $(u^3 = u_{yx} + u_{xy})$ . We first analysed profiles of the local shear-elongation angle  $\alpha_s(\phi) = \arg(u^2 + iu^3)/2$  (Fig. 4a, inset) measured at different lattice sites (Fig. 4a) surrounding a defect pair. In a general isotropic linearly elastic solid,  $\alpha(\phi)$  is independent of the distance from the defect<sup>6</sup> and in a conventional passive solid, where all moduli except B and  $\mu$  vanish,  $\alpha_s$  is parameter free<sup>6</sup> (dashed line, Fig. 4b). In contrast, our measured values of  $\alpha_s$  (Fig. 4b, grey dots) averaged at lattice sites (black symbols) show a more complex pattern that can only be explained by allowing for a more exotic material response that may include non-vanishing odd moduli<sup>6</sup> (solid line in Fig. 4b and Supplementary Section 3.11.4). We then fit in a second step the full spatial profiles of the shear-strain components  $u^2$  and  $u^3$  (Supplementary Section 3.11.5), which yields results consistent with the shear-angle analysis (Fig. 4b), and in addition provides the relative odd moduli estimates  $A/\mu \approx 8$  and  $K^{\circ}/\mu \approx 7$ . Finally, we validate these fit results by predicting the remaining strain components  $u^0$  and  $u^1$  (Fig. 4c, top) that had not been used so far and find very good quantitative agreement with experiments (Fig. 4c, bottom).

The presence of odd moduli raises the possibility that LCCs can support self-sustained chiral waves and strain cycles, similar to those recently predicted in odd elastic materials $^5$ . In the displacement fields  $\mathbf{u}(\mathbf{r}_i,t)$  introduced above, we indeed observe the propagation of chiral displacement waves (Fig. 4d and Supplementary Sections 3.9 and 3.10) that persist for more than an hour (Supplementary Videos 6–8). The existence of such waves in an overdamped LCC is a direct manifestation of its non-equilibrium nature. The frequency of the dominant, chiral modes (Supplementary Fig. 10), 0.28 min $^{-1}$ , is close to the spinning frequency of individual embryos within the cluster, 0.33 min $^{-1}$  (Supplementary Section 3.4), suggesting that these modes are directly linked to the spinning motion of embryos.

A generic feature of systems with non-reciprocal interactions is that mechanical work can be extracted from quasistatic cyclic processes. Specifically, in materials with an odd elastic response, work can be extracted from cyclic deformations (strain cycles)<sup>5</sup> (Supplementary Section 2.3.1). To investigate whether strain cycles exist in an LCC, we determined the displacement gradient tensor,  $u_{ij} = \partial_i u_i$  with  $i, j \in \{x, y\}$ . As evident from kymographs measured along the boundary (Fig. 4e,g) and in the bulk (Supplementary Section 3.9) of the LCC, all strain components exhibit long-lived oscillations that span the whole cluster (Supplementary Video 9). Moreover, in the space of suitable strain component pairs (insets in Fig. 4f,h), strain cycles are found that have the same handedness almost everywhere in the cluster (Supplementary Section 3.12.2). Such strain cycles are theoretically predicted as part of the chiral waves that odd elastic solids can support<sup>5</sup>. Together with the signs of the measured odd moduli, A and  $K^{\circ} > 0$ , we conclude that oscillating LCCs are effectively doing work on the surrounding fluid (Supplementary Section 2.3.1).

Strain waves in materials with finite odd elastic moduli can give rise to work and dissipation cycles<sup>5</sup>. To quantify the lower bounds of the associated entropy production rates, we estimated the statistical irreversibility of strain cycles using recently developed frameworks of stochastic thermodynamics<sup>41,42</sup>. By calculating the local phase-space currents in strain space (Supplementary Section 3.12), we constructed spatial maps of the local entropy production rates arising in the relevant strain component spaces (Fig. 4f,h and Supplementary Video 10). These maps reveal spatio-temporal variations of the entropy production rates, with higher rates appearing mostly in the vicinity of vacancy defects and boundary regions. Spatially integrated entropy production rates exhibit in both spaces temporal maxima during the period of most active wave propagation (Supplementary Fig. 15).

#### Discussion

Our combined experimental and theoretical results demonstrate how morphological changes in developing multicellular organisms can lead to the self-assembly and dissolution of living crystals with broken chiral symmetry. By observing starfish embryos over two days post gastrulation, we have identified hydrodynamic and morphological single-embryo properties that facilitate these self-organized processes. Over the course of several hours, thousands of embryos can come together to form a macroscopic non-equilibrium material that carries signatures of odd elasticity. Driven by the embryos' inherent activity, these living crystal structures support self-sustained chiral waves that exemplify upwards energy transport from the individual microscopic constituents to the macroscale. More broadly, such living chiral crystals can serve as a paradigmatic active-matter system to elucidate the principles of collective self-organization, non-equilibrium thermodynamics and exotic material properties that emerge from non-reciprocal interactions.

#### **Online content**

Any methods, additional references, Nature Research reporting summaries, source data, extended data, supplementary information, acknowledgements, peer review information; details of author contributions and competing interests; and statements of data and code availability are available at https://doi.org/10.1038/s41586-022-04889-6.

- Palacci, J., Sacanna, S., Preska Steinberg, A., Pine, D. J. & Chaikin, P. M. Living crystals of light-activated colloidal surfers. Science 339, 936–940 (2013).
- Billilign, E. S. et al. Motile dislocations knead odd crystals into whorls. Nat. Phys. 18, 212–218 (2022).
- Petroff, A. P., Wu, X.-L. & Libchaber, A. Fast-moving bacteria self-organize into active two-dimensional crystals of rotating cells. Phys. Rev. Lett. 114, 158102 (2015).
- Petroff, A. P. & Libchaber, A. Nucleation of rotating crystals by *Thiovulum majus* bacteria. New J. Phys. 20, 015007 (2018).
- Scheibner, C. et al. Odd elasticity. Nat. Phys. 16, 475–480 (2020).
- Braverman, L., Scheibner, C., VanSaders, B. & Vitelli, V. Topological defects in solids with odd elasticity. Phys. Rev. Lett. 127, 268001 (2021).
- Anderson, P. W. More is different. Science 177, 393-396 (1972).
- Ashcroft, N. W. & Mermin, N. D. Solid State Physics (Saunders College Publishing/ Harcourt College Publishers, 1976).
- Li, R. & Bowerman, B. Symmetry breaking in biology. Cold Spring Harb. Perspect. Biol. 2, a003475 (2010).
- Bricard, A., Caussin, J.-B., Desreumaux, N., Dauchot, O. & Bartolo, D. Emergence of macroscopic directed motion in populations of motile colloids. *Nature* 503, 95–98 (2013).
- Grzybowski, B. A., Stone, H. A. & Whitesides, G. M. Dynamic self-assembly of magnetized, millimetre-sized objects rotating at a liquid-air interface. *Nature* 405, 1033–1036 (2000).
- Lee, W., Amini, H., Stone, H. A. & Di Carlo, D. Dynamic self-assembly and control of microfluidic particle crystals. Proc. Natl Acad. Sci. USA 107, 22413–22418 (2010).
- Naganathan, S. R., Fürthauer, S., Nishikawa, M., Jülicher, F. & Grill, S. W. Active torque generation by the actomyosin cell cortex drives left-right symmetry breaking. eLife 3, eO4165 (2014).
- Smith, D. J., Montenegro-Johnson, T. D. & Lopes, S. S. Symmetry-breaking cilia-driven flow in embryogenesis. *Annu. Rev. Fluid Mech.* 51, 105–128 (2019).
- Riedel, I. H., Kruse, K. & Howard, J. A self-organized vortex array of hydrodynamically entrained sperm cells. Science 309, 300–303 (2005).
- Sokolov, A., Aranson, I. S., Kessler, J. O. & Goldstein, R. E. Concentration dependence of the collective dynamics of swimming bacteria. *Phys. Rev. Lett.* 98, 158102 (2007).

- Shen, Z., Würger, A. & Lintuvuori, J. S. Hydrodynamic self-assembly of active colloids: chiral spinners and dynamic crystals. Soft Matter 15, 1508-1521 (2019).
- 18. Bäuerle, T., Löffler, R. C. & Bechinger, C. Formation of stable and responsive collective states in suspensions of active colloids. Nat. Commun. 11, 2547 (2020).
- Koch, A.-J. & Meinhardt, H. Biological pattern formation: from basic mechanisms to complex structures. Rev. Mod. Phys. 66, 1481-1507 (1994).
- Wang, G. et al. Emergent field-driven robot swarm states. Phys. Rev. Lett. 126, 108002
- 21. Omar, A. K., Klymko, K., GrandPre, T. & Geissler, P. L. Phase diagram of active brownian spheres: crystallization and the metastability of motility-induced phase separation. Phys. Rev. Lett. 126, 188002 (2021).
- 22. Avron, J. E. Odd viscosity. J. Stat. Phys. 92, 543-557 (1998).
- Soni, V. et al. The odd free surface flows of a colloidal chiral fluid. Nat. Phys. 15, 1188-1194 23. (2019).
- Banerjee, D., Vitelli, V., Jülicher, F. & Surówka, P. Active viscoelasticity of odd materials. 24. Phys. Rev. Lett. 126, 138001 (2021).
- 25. Christina Marchetti, M. et al. Hydrodynamics of soft active matter. Rev. Mod. Phys. 85, 1143-1189 (2013).
- Shankar, S., Souslov, A., Bowick, M. J., Cristina Marchetti, M. & Vitelli, V. Topological active 26. matter. Nat. Rev. Phys. 4, 380-398 (2022).
- 27 Cates, M. E. & Tailleur, J. Motility-induced phase separation. Annu. Rev. Condens. Matter Phys. 6, 219-244 (2015).
- 28 Bi, D., Lopez, J. H., Schwarz, J. M. & Manning, M. L. A density-independent rigidity transition in biological tissues. Nat. Phys. 11, 1074-1079 (2015).
- 29. Hartmann, R. et al. Emergence of three-dimensional order and structure in growing biofilms. Nat. Phys. 15, 251 (2019).
- Qin, B. et al. Cell position fates and collective fountain flow in bacterial biofilms revealed by light-sheet microscopy. Science 369, 71-77 (2020).
- Collinet, C. & Lecuit, T. Programmed and self-organized flow of information during morphogenesis. Nat. Rev. Mol. Cell Biol. 22, 245-265 (2021).

- Rosenthal, S. B., Twomey, C. R., Hartnett, A. T., Wu, H. S. & Couzin, I. D. Revealing the hidden networks of interaction in mobile animal groups allows prediction of complex behavioral contagion. Proc. Natl Acad. Sci. USA 112, 4690-4695 (2015).
- 33. Bialek, W. et al. Statistical mechanics for natural flocks of birds. Proc. Natl Acad. Sci. USA 109, 4786-4791 (2012).
- 34. Drescher, K. et al. Dancing volvox: hydrodynamic bound states of swimming algae. Phys. Rev. Lett. 102, 168101 (2009).
- 35. Lauga, E. The Fluid Dynamics of Cell Motility (Cambridge Texts in Applied Mathematics, Cambridge Univ. Press, 2020).
- 36. Gilpin, W., Prakash, V. N. & Prakash, M. Vortex arrays and ciliary tangles underlie the feeding-swimming trade-off in starfish larvae. Nat. Phys. 13, 380-386 (2017).
- Wan, K. Y. et al. Reorganization of complex ciliary flows around regenerating Stentor coeruleus. Phil. Trans. R. Soc. B 375, 20190167 (2020).
- 38. Ishikawa, T., Pedley, T. J., Drescher, K. & Goldstein, R. E. Stability of dancing Volvox. J. Fluid Mech. 903, A11 (2020).
- 39. Nelson, D. R. & Halperin, B. I. Dislocation-mediated melting in two dimensions, Phys. Rev. B 19, 2457 (1979).
- 40. Zahn, K. & Maret, G. Dynamic criteria for melting in two dimensions, Phys. Rev. Lett. 85. 3656 (2000).
- Battle, C. et al. Broken detailed balance at mesoscopic scales in active biological 41. systems. Science 352, 604-607 (2016).
- 42. Li, J., Horowitz, J. M., Gingrich, T. R. & Fakhri, N. Quantifying dissipation using fluctuating currents, Nat. Commun. 10, 1666 (2019).
- 43. Reuther, A. et al. Interactive supercomputing on 40,000 cores for machine learning and data analysis. IEEE High Perf. Ext. Comp. Conf. 1, 1-6 (2018).

Publisher's note Springer Nature remains neutral with regard to jurisdictional claims in published maps and institutional affiliations.

© The Author(s), under exclusive licence to Springer Nature Limited 2022

## Data availability

All data that support the plots within this paper and other findings of this study are available from the corresponding author upon reasonable request.

## **Code availability**

The computational methods that support the plots within this paper are described in the Supplementary Information and the underlying code is available from the corresponding author upon reasonable request.

Acknowledgements We thank C. Scheibner, W. Irvine, N. Wingreen, J. Liu, Y.-C. Chao and R. E. Goldstein for valuable discussions. This research was supported by a Sloan Foundation Grant (G-2021-16758) to N.F. and J.D., and a National Science Foundation CAREER Award to N.F. T.H.T. acknowledges support from the NSF-Simons Center for Mathematical and Statistical Analysis of Biology at Harvard (award number 1764269) and Harvard Quantitative Biology Initiative as an NSF-Simons Postdoctoral Fellow. T.H.T. acknowledges support from the Center for Systems Biology Dresden as ELBE Postdoctoral Fellow. A.M. acknowledges support from a Longterm Fellowship from the European Molecular Biology Organization (ALTF 528-2019) and a Postdoctoral Research Fellowship from the Deutsche Forschungsgemeinschaft (Project

431144836). Y.C. acknowledges support from MIT Department of Physics Curtis Marble Fellowship. P.J.F. and S.G. acknowledge support from the Gordon and Betty Moore Foundation as Physics of Living Systems Fellows through grant no. GBMF4513. J.D. was supported by the Robert E. Collins Distinguished Scholarship fund. N.F., J.D. and S.G. are grateful to the KITP programme ACTIVE20: Symmetry, Thermodynamics and Topology in Active Matter, supported in part by the National Science Foundation under grant no. NSF PHY-1748958. We thank the MIT SuperCloud<sup>43</sup> for providing access to its HPC resources.

Author contributions N.F., J.D., T.H.T. and A.M. conceived the project. T.H.T. and A.M. are joint first authors. J.L. and Y.C. are joint second authors. T.H.T. designed and performed experiments and analysed data. A.M. developed the theory, performed simulations and analysed data. J.L. performed experiments and analysed data. Y.C. analysed data. H.H. performed experiments. P.J.F. performed experiments and analysed data. S.G. analysed data. N.F. and J.D. designed experiments and theory and supervised research. All authors discussed the results and co-wrote the paper.

Competing interests The authors declare no competing interests.

#### Additional information

**Supplementary information** The online version contains supplementary material available at https://doi.org/10.1038/s41586-022-04889-6.

Correspondence and requests for materials should be addressed to Nikta Fakhri. Peer review information Nature thanks Vivek Prakash, Anton Souslov and the other, anonymous, reviewer(s) for their contribution to the peer review of this work. Reprints and permissions information is available at http://www.nature.com/reprints.